Research Article Vol. 28, No. 2 / 20 January 2020 / Optics Express 1061
Optics EXPRESS

Large depth-of-field tracking of colloidal spheres in holographic microscopy by modeling the objective lens

BRIAN LEAHY,[1,3] RONALD ALEXANDER,[2,3] CAROLINE MARTIN,[1] SOLOMON BARKLEY,[2] AND VINOTHAN N. MANOHARAN[1,2,*]

[1]Harvard John A. Paulson School of Engineering and Applied Sciences, Harvard University, Cambridge, MA 02138, USA
[2]Department of Physics, Harvard University, Cambridge, MA 02138, USA
[3]These authors contributed equally to this work
[*]vnm@seas.harvard.edu

Abstract: Holographic microscopy has developed into a powerful tool for 3D particle tracking, yielding nanometer-scale precision at high frame rates. However, current particle tracking algorithms ignore the effect of the microscope objective on the formation of the recorded hologram. As a result, particle tracking in holographic microscopy is currently limited to particles well above the microscope focus. Here, we show that modeling the effect of an aberration-free lens allows tracking of particles above, near, and below the focal plane in holographic microscopy, doubling the depth of field. Finally, we use our model to determine the conditions under which ignoring the effect of the lens is justified and in what conditions it leads to systematic errors.

1. Introduction

Digital holographic microscopy excels at fast, precise three-dimensional (3D) imaging of colloidal particles and nanoparticles. In a typical in-line digital holographic microscope, coherent light illuminates a sample, an objective collects the scattered and transmitted light, and a digital camera records the resulting interference pattern, or hologram (Fig. 1(a)). Compared to bright-field and confocal microscopy, holographic microscopy has three advantages for imaging small particles. First, because a hologram records both the phase and amplitude of the scattered wave, a single camera exposure captures information about the particles' 3D position, shape, and size. Second, because the technique does not require fluorescent labels, the incident beam power is not limited by bleaching. Third, the depth of field in holography is tens to hundreds of micrometers. Combined, these three advantages give holographic microscopy an enormous dynamic range: 3D information can be captured at rates of thousands of frames per second and over durations of hours or more. Moreover, the precision of the technique is unparalleled: micrometer-sized particles can be localized to nanometer-scale precision in all three dimensions [1]. Holographic microscopes have been used to track both individual colloidal particles [2,3] and colloidal clusters [4] in 3D, to watch colloidal particles breach interfaces [5], and to characterize 3D fluid turbulence [6,7]. Because it is noninvasive, holographic microscopy has also proven useful for imaging living specimens, including bacterial [8] and eukaryotic cells [9–12].

Extracting 3D information about the sample, such as the 3D position of a particle, requires analyzing the recorded hologram. One method, based on Gabor's original conception of holography [13], is to reconstruct the electric field everywhere in space using the phase and amplitude information recorded in the hologram and to identify the particle's location from the reconstructed field [14]. This approach is indirect: the hologram is processed to yield a reconstruction of the field, which is then processed again to extract the particle's position.

#382159 https://doi.org/10.1364/OE.382159
Journal © 2020 Received 4 Nov 2019; revised 13 Dec 2019; accepted 13 Dec 2019; published 6 Jan 2020

Optics EXPRESS

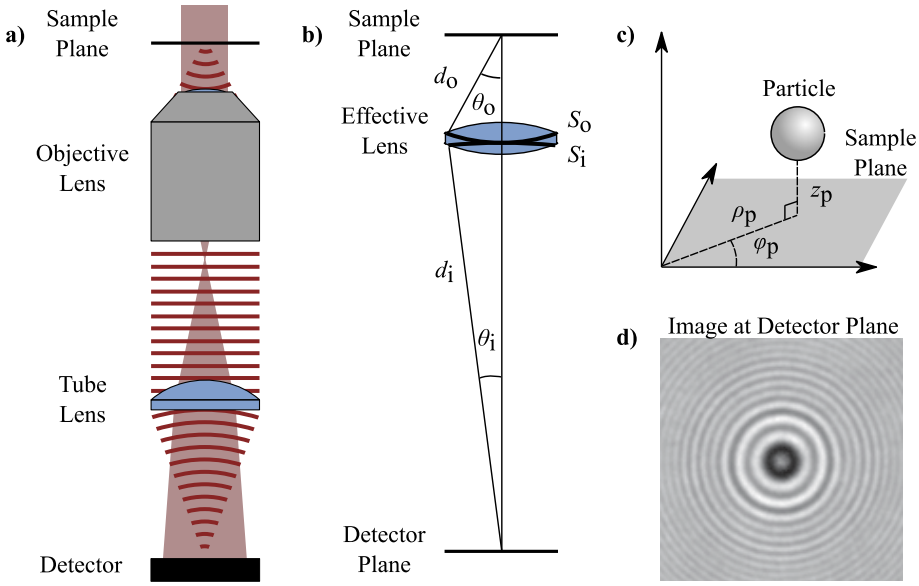

Fig. 1. (a) In in-line digital holographic microscopy, a collimated laser (light red) illuminates a sample, which scatters light (dark red wavefronts). A microscope objective collects the transmitted and some of the scattered light, and a tube lens focuses this light onto a digital camera. (b) We treat the objective and tube lens combination as a single effective lens. The thick lines illustrate the Gaussian reference spheres S_o and S_i. The thin lines illustrate the coordinates (d_o, θ_o) and (d_i, θ_i) in one plane; the coordinates ϕ_o and ϕ_i describe the rotation about the optical axis. (c) The coordinate system for the particle position relative to the objective's focus. (d) A recorded hologram of a polystyrene sphere.

Furthermore, the depth resolution is poor [15], and artifacts arise when the particle is comparable in size to the wavelength of the incident light [16].

A more direct and precise approach is forward modeling combined with inference, wherein the recorded hologram is compared to a simulation from a scattering model [1,17,18]. The parameters of the model—which might include the particle's position, size, and refractive index—can then be determined by fitting the simulated hologram to the measured one. With this approach, one can not only track particles with high precision [5,19,20] but also calculate uncertainties on the particle positions using Bayesian inference [21].

Although many forward models start from exact solutions of Maxwell's equations to describe the particle scattering [3,22,23], modeling the hologram formation from the scattered wave involves approximations that ultimately limit our ability to track particles. In most approaches, the hologram $H(\mathbf{x}_p)$ recorded on the detector is modeled as the magnified image of the scattered field $\mathbf{E}_{sc}$ and the incident field $\mathbf{E}_{in}$ at the focal plane of the objective:

$$H(\mathbf{x}_p) = \left|\mathbf{E}_{in} + \alpha \mathbf{E}_{sc}(\mathbf{x}_p)\right|^2, \tag{1}$$

where $\mathbf{x}_p$ is the particle's position relative to the point in the focal plane conjugate to a detector pixel, and α is a field-rescaling parameter that accounts for experimental imperfections in the optical setup [1]. When the particle is well above the focal plane, this *lensless model* works well. However, when the particle is near or below the focal plane, the lensless model makes the unphysical prediction that the hologram results from the internal or backscattered electric field. Accordingly, the lensless model is not useful for tracking the motion of particles near or below the focus of the objective; therefore, this approximation limits the depth of field. Furthermore,

Optics EXPRESS

the lensless model does not account for physical effects of the lens such as the Gouy phase shift [24–27]. As we shall show, modeling these effects is critical to accurately simulating the hologram when the particle is near the focus.

Here we show that explicitly modeling the effects of the objective lens doubles the depth of field of the holographic microscope by reducing systematic errors near and below the objective's focus. We model the lens by describing the scattered electric field as defocused, forward-scattered light, in an approach similar to that of [17] but with additional simplifications that allow for a compact representation of the recorded hologram. With this model, we can track particles above, near, and below the focus of the objective. Finally, by comparing the results of our model to the lensless model, we determine the conditions under which the lens can be safely ignored.

2. Theory

To create an analytically tractable model for the effect of the lens, we simplify the full optical train of an inline holographic microscope. First, we ignore any reflections or aberrations due to the optical interface of the cover slip [17,28], because these can be minimized with an immersion lens. Second, we describe the combination of the objective and tube lens as a single effective lens with the same magnification and numerical aperture, because this is the simplest model that captures the phase, polarization, and resolution effects of the imaging system [29]. Third, we assume an aberration-free and translationally invariant aplanatic system, which is a good approximation for modern microscope lenses. This simplified model of the imaging system is shown in Fig. 1(b).

To calculate the hologram on the detector plane, we treat the scattered beam and the incident beam separately. We calculate the image of the scattered field following derivations of microscope point-spread functions [28–30]. In Sec. 2.1, we evaluate the scattered electric field on the lens's entrance pupil, represented as a Gaussian reference sphere S_o of radius d_o centered on the object point of the effective lens. In Sec. 2.2, we model how the lens transforms the field on its entrance pupil to that on its exit pupil, represented as the Gaussian reference sphere S_i of radius d_i centered on the image point of the effective lens. In Sec. 2.3, we use a diffraction integral to propagate the scattered field from the surface S_i to the detector plane. This step yields a two-dimensional integral equation for the field scattered from a generic particle as imaged through a large-aperture microscope objective. In Sec. 2.4, we simplify this integral for spherically symmetric scatterers, reducing it to a one-dimensional integral that is easily evaluated numerically. Finally, in Sec. 2.5, we model the hologram by calculating the interference between the scattered field and the transmitted field, which propagates through the same optical train.

We work in physical limits relevant for holographic microscopy. We assume that the microscope dimensions are large compared to the wavelength of light ($kd_o \gg 1$, $kd_i \gg 1$, where k is the wavevector of the light in the medium); that the position of the particle $\mathbf{x}_p$ is close to the focus of the imaging system ($|\mathbf{x}_p|/d_o \ll 1$); and that the ratio of the microscope's numerical aperture NA to its magnification M is small—an assumption equivalent to $\theta_i \ll 1$, where θ_i is defined in Fig. 1(b). For a 100× magnification, NA = 1.0 microscope with a working distance of 0.2 mm and a 200 mm tube lens that images a particle 5 μm from its focal plane using 660 nm red light, $kd_o \approx 2 \times 10^3$, $kd_i \approx 2 \times 10^6$, $|\mathbf{x}_p|/d_o \approx 0.02$, and $\mathrm{NA}/M \approx 0.01$, and these approximations are well justified. We allow the numerical aperture to be large and do not make a paraxial approximation.

2.1. Scattered field on the entrance pupil of the lens

We first evaluate the electric field on the Gaussian reference sphere S_o, as scattered from a particle located at a position $\mathbf{x}_p$ from the center of S_o (see Fig. 1(b) for a coordinate diagram). Let $\mathbf{d}_o$ be a point on S_o, which we represent in spherical polar coordinates from the center of S_o as (d_o, θ_o, ϕ_o). The point $\mathbf{d}_o$ is located at $\mathbf{r}_{op} \equiv \mathbf{d}_o - \mathbf{x}_p$ relative to the particle. Because the lens is a macroscopic

Optics EXPRESS

distance from the particle, the magnitude of $\mathbf{r}_{\mathrm{op}}$ is much larger than the wavelength of light, and the scattered electric field on S_{o} is in the far-field limit. For a generic scatterer excited by an incoming wave $E_0\hat{\mathbf{x}}e^{ikz}$, the scattered electric field in the far-field limit takes the form [31]

$$\mathbf{E}_{S_{\mathrm{o}}} = \frac{E_0}{ikr_{\mathrm{op}}} e^{-ikr_{\mathrm{op}}+ikz_{\mathrm{p}}}\, \boldsymbol{S}(\theta_{\mathrm{op}}, \phi_{\mathrm{op}}) \cdot \hat{\mathbf{x}}, \tag{2}$$

where $(r_{\mathrm{op}}, \theta_{\mathrm{op}}, \phi_{\mathrm{op}})$ is the decomposition of $\mathbf{r}_{\mathrm{op}}$ in spherical polar coordinates and $\boldsymbol{S}$ is the far-field scattering matrix. To lowest order in $|\mathbf{x}_{\mathrm{p}}|/d_{\mathrm{o}}$, these components are $r_{\mathrm{op}} = d_{\mathrm{o}} - \mathbf{x}_{\mathrm{p}} \cdot \mathbf{d}_o/d_{\mathrm{o}}$, $\theta_{\mathrm{op}} = \theta_{\mathrm{o}}$, and $\phi_{\mathrm{op}} = \phi_{\mathrm{o}}$, and the scattered field on the surface S_{o} is

$$\mathbf{E}_{S_{\mathrm{o}}}(d_{\mathrm{o}}, \theta_{\mathrm{o}}, \phi_{\mathrm{o}}) = \frac{E_0}{ikd_{\mathrm{o}}} e^{-ikd_{\mathrm{o}}} e^{ik\rho_{\mathrm{p}} \sin\theta_{\mathrm{o}} \cos(\phi_{\mathrm{o}}-\phi_{\mathrm{p}})} e^{ikz_{\mathrm{p}}(1-\cos\theta_{\mathrm{o}})}\, \boldsymbol{S}(\theta_{\mathrm{o}}, \phi_{\mathrm{o}}) \cdot \hat{\mathbf{x}}, \tag{3}$$

where $(\rho_{\mathrm{p}}, \phi_{\mathrm{p}}, z_{\mathrm{p}})$ is the particle position in cylindrical coordinates, with $+z_{\mathrm{p}}$ oriented away from the lens. The paraxial approximation differs from Eq. (3) by making the approximations $\sin\theta_{\mathrm{o}} \approx \theta_{\mathrm{o}}$ and $\cos\theta_{\mathrm{o}} \approx 1$. We do not use the paraxial approximation because the scattered field in this approximation does not provide any information about the particle's axial position z_{p}.

2.2. Transformation of the scattered field by the lens

The lens transforms the phase, polarization direction, and magnitude of the scattered field on S_{o} to new values on S_{i}. To understand this transformation, we consider a simple model of a perfect lens [29,30]. A perfect lens stigmatically images a point at the object plane to a point on the image plane; all rays from the object point which enter the lens pupil intersect at the image point. By Fermat's principle, each of these rays traverses an equal optical path. Since the surface S_{o} is a sphere centered at the object point, each ray leaving the object point accumulates the same phase at S_{o}. Likewise, each ray leaving the second spherical surface S_{i} accumulates the same phase at the image point. Thus, to stigmatically image the object point to the image point, the lens maps the rays on the first surface S_{o} to the second surface S_{i} with the same constant phase shift Φ for each ray.

The lens also rotates the electric field's polarization, applying the same rotation to the polarization vectors as it does to the ray directions [32]. The lens rotates the polarization projection along the unit vector $\hat{\theta}_{\mathrm{o}}$ on S_{o} to along $\hat{\theta}_{\mathrm{i}}$ on S_{i}, and from $\hat{\phi}_{\mathrm{o}}$ to $\hat{\phi}_{\mathrm{i}}$, where $(\theta_{\mathrm{i}}, \phi_{\mathrm{i}})$ are coordinates on the surface S_{i}, and $(\hat{\theta}_{\mathrm{i}}, \hat{\phi}_{\mathrm{i}})$ are the associated unit vectors. For a typical microscope imaging configuration, $d_{\mathrm{i}} \gg d_{\mathrm{o}}$, and the polarization vectors exiting the lens will be approximately parallel to the detector plane—that is, $\hat{\theta}_{\mathrm{i}} \approx \hat{\mathbf{x}} \cos\phi_{\mathrm{i}} + \hat{\mathbf{y}} \sin\phi_{\mathrm{i}}$ and $\hat{\phi}_{\mathrm{i}} \approx -\hat{\mathbf{x}} \sin\phi_{\mathrm{i}} + \hat{\mathbf{y}} \cos\phi_{\mathrm{i}}$.

Finally, the lens slightly rescales the magnitude of the electric field as the rays propagate from S_{o} to S_{i} [29]. Consider the flux of energy from the rays that enter through a small surface area dS_{o} centered at $(\theta_{\mathrm{o}}, \phi_{\mathrm{o}})$ on the entrance pupil and exit through the area dS_{i} on the exit pupil. By conservation of energy, the incident flux $|E_{S_{\mathrm{o}}}|^2/c \times dS_{\mathrm{o}}$ must equal the outgoing flux $|E_{S_{\mathrm{i}}}|^2/c \times dS_{\mathrm{i}}$. For a translationally-invariant aplanatic system of magnification M, the Abbe sine condition, $\sin\theta_{\mathrm{o}} = M \sin\theta_{\mathrm{i}}$, relates the two elements of area as $\cos\theta_{\mathrm{i}} dS_{\mathrm{i}} = \cos\theta_{\mathrm{o}} dS_{\mathrm{o}}$. Substituting this relation into the outgoing flux and approximating $\cos\theta_{\mathrm{i}} \approx 1$ relates the field magnitudes as $|\mathbf{E}_{S_{\mathrm{i}}}| = |\mathbf{E}_{S_{\mathrm{o}}}|/\sqrt{\cos\theta_{\mathrm{o}}}$.

Combining the phase shift, polarization rotation, and the change in magnitude due to the lens yields the field on the exit pupil S_{i}:

$$\begin{aligned}\mathbf{E}_{S_{\mathrm{i}}}(\theta_{\mathrm{i}}, \phi_{\mathrm{i}}) = e^{i\Phi} \frac{1}{\sqrt{\cos\theta_{\mathrm{o}}}} \Big[&\left(\hat{\theta}_{\mathrm{o}} \cdot \mathbf{E}_{S_{\mathrm{o}}}(\theta_{\mathrm{o}}, \phi_{\mathrm{o}})\right)(\hat{\mathbf{x}} \cos\phi_{\mathrm{i}} + \hat{\mathbf{y}} \sin\phi_{\mathrm{i}}) + \\ &\left(\hat{\phi}_{\mathrm{o}} \cdot \mathbf{E}_{S_{\mathrm{o}}}(\theta_{\mathrm{o}}, \phi_{\mathrm{o}})\right)(-\hat{\mathbf{x}} \sin\phi_{\mathrm{i}} + \hat{\mathbf{y}} \cos\phi_{\mathrm{i}}) \Big].\end{aligned} \tag{4}$$

Optics EXPRESS

2.3. Propagation of the scattered field to detector plane

Finally, the electric field propagates from S_i to the detector. For a translationally-invariant optical system, we need only consider the electric field at the detector's center, corresponding to the center of the sphere S_i, because examining a different location on the detector is equivalent to shifting the particle. A Kirchoff diffraction integral over the surface S_i yields the scattered field at the center of the detector plane:

$$\mathbf{E}_{\mathrm{sc,det}} = \frac{ikd_\mathrm{i}}{4\pi} e^{-ikd_\mathrm{i}} \int (1+\cos\theta_\mathrm{i}) \mathbf{E}_{S_\mathrm{i}}\, d\Omega_\mathrm{i}, \tag{5}$$

where $d\Omega_\mathrm{i}$ is the element of solid angle on S_i. Here, the Green's function $ik/4\pi r \times e^{-ikr}$ is constant, because every point on the spherical cap S_i is a distance d_i from the focus of the imaging system. Substituting Eqs. (3) and (4) into Eq. (5), approximating $\cos\theta_\mathrm{i} \approx 1$, and transforming the domain of integration from S_i to S_o using the Abbe sine condition for the Jacobian $d\Omega_\mathrm{i}/d\Omega_\mathrm{o}$ yields the scattered electric field at the detector:

$$\begin{aligned}\mathbf{E}_{\mathrm{sc,det}} =& \frac{1}{2\pi}\frac{E_0}{M} e^{-ikd_\mathrm{i}} e^{i\Phi} e^{-ikd_\mathrm{o}} \times \\ & \int_{\phi_\mathrm{o}=0}^{2\pi}\int_{\theta_\mathrm{o}=0}^{\beta} e^{ik\rho_\mathrm{p}\sin\theta_\mathrm{o}\cos(\phi_\mathrm{o}-\phi_\mathrm{p})} e^{ikz_\mathrm{p}(1-\cos\theta_\mathrm{o})} \times \\ & \Big[\left(\hat{\theta}_\mathrm{o}\cdot\boldsymbol{S}(\theta_\mathrm{o},\phi_\mathrm{o})\cdot\hat{\mathbf{x}}\right)(\hat{\mathbf{x}}\cos\phi_\mathrm{o}+\hat{\mathbf{y}}\sin\phi_\mathrm{o}) + \\ & \left(\hat{\phi}_\mathrm{o}\cdot\boldsymbol{S}(\theta_\mathrm{o},\phi_\mathrm{o})\cdot\hat{\mathbf{x}}\right)(-\hat{\mathbf{x}}\sin\phi_\mathrm{o}+\hat{\mathbf{y}}\cos\phi_\mathrm{o}) \Big] \sqrt{\cos\theta_\mathrm{o}}\,\sin\theta_\mathrm{o}\, d\theta_\mathrm{o} d\phi_\mathrm{o},\end{aligned} \tag{6}$$

where β is the acceptance angle of the objective, related to the numerical aperture NA through the immersion fluid index n_f as $\mathrm{NA} = n_f \sin\beta$. Equation (6) gives the electric field from an arbitrary scatterer as imaged on the detection plane of a microscope.

2.4. Simplified form for Mie scatterers

Up to this point, we have made no assumptions about the type of scatterer. For spherically symmetric scatterers, the symmetry of the scattered field greatly simplifies Eq. (6), allowing us to analytically integrate over the ϕ coordinate. The far-field scattering matrix becomes

$$\boldsymbol{S}(\theta_\mathrm{o},\phi_\mathrm{o})\cdot\hat{\mathbf{x}} = S_\parallel(\theta_\mathrm{o})\cos(\phi_\mathrm{o})\hat{\theta}_\mathrm{o} - S_\perp(\theta_\mathrm{o})\sin(\phi_\mathrm{o})\hat{\phi}_\mathrm{o}, \tag{7}$$

where $S_\parallel$ and $S_\perp$ are given by Mie theory [31]. Substituting the scattered field into Eq. (6) yields integrals over ϕ_o of the form $\int_0^{2\pi}\cos(n\phi_\mathrm{o})e^{ix\cos\phi_\mathrm{o}}\,d\phi_\mathrm{o}$ and $\int_0^{2\pi}\sin(n\phi_\mathrm{o})e^{ix\cos\phi_\mathrm{o}}\,d\phi_\mathrm{o}$, which can be evaluated analytically as Bessel functions. Doing so yields the image of the scattered field at the detector plane as a function of the sphere's position $\mathbf{x}_p$ in cylindrical coordinates:

$$\begin{aligned}\mathbf{E}_{\mathrm{sc,det}}(\rho_\mathrm{p},\phi_\mathrm{p},z_\mathrm{p}) =& \frac{1}{2}\frac{E_0}{M} e^{-ikd_\mathrm{i}} e^{i\Phi} e^{-ikd_\mathrm{o}} \times \\ & \left\{ \left[\mathcal{I}_0(k\rho_\mathrm{p},kz_\mathrm{p}) + \mathcal{I}_2(k\rho_\mathrm{p},kz_\mathrm{p})\cos(2\phi_\mathrm{p})\right]\hat{\mathbf{x}} + \mathcal{I}_2(k\rho_\mathrm{p},kz_\mathrm{p})\sin(2\phi_\mathrm{p})\hat{\mathbf{y}} \right\},\end{aligned} \tag{8}$$

where we define the integrals $\mathcal{I}_0$ and $\mathcal{I}_2$ as

$$\mathcal{I}_0(u,v) = \int_0^\beta \left[S_\perp(\theta_\mathrm{o}) + S_\parallel(\theta_\mathrm{o})\right] J_0(u\sin\theta_\mathrm{o}) e^{iv(1-\cos\theta_\mathrm{o})} \sqrt{\cos\theta_\mathrm{o}}\sin\theta_\mathrm{o}\, d\theta_\mathrm{o} \tag{9}$$

$$\mathcal{I}_2(u,v) = \int_0^\beta \left[S_\perp(\theta_\mathrm{o}) - S_\parallel(\theta_\mathrm{o})\right] J_2(u\sin\theta_\mathrm{o}) e^{iv(1-\cos\theta_\mathrm{o})} \sqrt{\cos\theta_\mathrm{o}}\sin\theta_\mathrm{o}\, d\theta_\mathrm{o}, \tag{10}$$

where J_n is the Bessel function of the first kind of order n.

Optics EXPRESS

2.5. Incident beam and hologram

The change to the incident beam as it passes through the lens is much simpler to evaluate. As the initially collimated incident beam propagates to the surface S_o, it accumulates a phase $\exp(-ikd_o)$. Since the incident beam strikes the lens axially, its polarization vector and amplitude are unchanged, and the lens only imparts a phase factor $\exp(i\Phi)$. On exiting, the incident beam passes through a focus at the back focal point of the lens, eventually accumulating a Gouy phase shift of -1 [26]. The beam continues to propagate to the detector plane, accumulating an additional phase shift of $\exp(-ikd_i)$. On striking the detector, the incident beam has a magnification of M, which decreases the magnitude of the field by $1/M$. Combining these effects, we find that the incident field at the detector plane is

$$\mathbf{E}_{\text{in,det}} = -\frac{E_0}{M} e^{-ikd_i} e^{i\Phi} e^{-ikd_o} \hat{\mathbf{x}}. \tag{11}$$

With the addition of the field-rescaling parameter α used to capture imperfections in the optical setup, the intensity recorded at the detector is proportional to $|\mathbf{E}_{\text{in,det}} + \alpha \mathbf{E}_{\text{sc,det}}|^2$. Absorbing the shared phase factors and constants into an overall scaling factor H_0 yields an expression for the recorded hologram:

$$\begin{aligned}\frac{H(\rho_p, \phi_p; z_p)}{H_0} = 1 - \alpha \text{Re}\left(\mathcal{I}_0(k\rho_p, kz_p) + \mathcal{I}_2(k\rho_p, kz_p)\cos 2\phi_p\right) + \\ \frac{\alpha^2}{4}\left|\mathcal{I}_0(k\rho_p, kz_p) + \mathcal{I}_2(k\rho_p, kz_p)\cos 2\phi_p\right|^2 + \frac{\alpha^2}{4}\left|\mathcal{I}_2(k\rho_p, kz_p)\right|^2 \sin^2 2\phi_p.\end{aligned} \tag{12}$$

Equation (12) is the basis of what we call the *lens model*, which predicts the hologram at a single point on the detector plane for a particle at an arbitrary position $\mathbf{x}_p$ from the conjugate point in the object plane. Calculating a hologram with the lens model is more straightforward than with the model of [17], in that it requires the evaluation of only two integrals $\mathcal{I}_0$ and $\mathcal{I}_2$ in Eqs. (9)–(10) and their combination in Eq. (12). Although derived for a point at the center of the detector, Eq. (12) is valid for any point on the detector plane, owing to the translational invariance of the imaging system. To calculate the hologram on the entire detector plane, we repeat this calculation, measuring the particle position $\mathbf{x}_p$ from the object point conjugate to each point on the detector plane.

3. Experimental results and discussion

To validate our model, we do an experiment in which we immobilize 1-μm-diameter polystyrene spheres in a gel and obtain holograms of an isolated particle as we sweep the microscope focus through it (see Appendix B). When the particle is far above the focal plane, the recorded hologram consists of a bright central lobe surrounded by rings (Fig. 2(a)). The ring spacing is primarily set by z_p and is visible as the cone-like structures in the xz-cross-section. As the particle approaches the focal plane, these rings come closer together, until the hologram becomes an image of the particle in focus. As the particle passes below the focus, the recorded hologram once again consists of rings centered on a central lobe with a spacing set primarily by the particle z_p, but with a dark rather than bright central lobe.

Both models predict holograms that agree with the experimental data when the particle is well above the focal plane (Figs. 2(b)–2(c)). However, as the particle nears the focus, the predictions of the lensless model start to deviate from the measurements. The lensless model is not designed to predict the hologram when the particle is at or below the focal plane, and in these regions, the lensless model produces unphysical predictions: it predicts that the hologram of a particle straddling the focus depends on the particle's internal field, and that of a particle below the focus depends on the back-scattered field. In contrast, the lens model uses only the forward-scattered light and generates holograms that agree with the experimental data over all particle z_p.

Optics EXPRESS

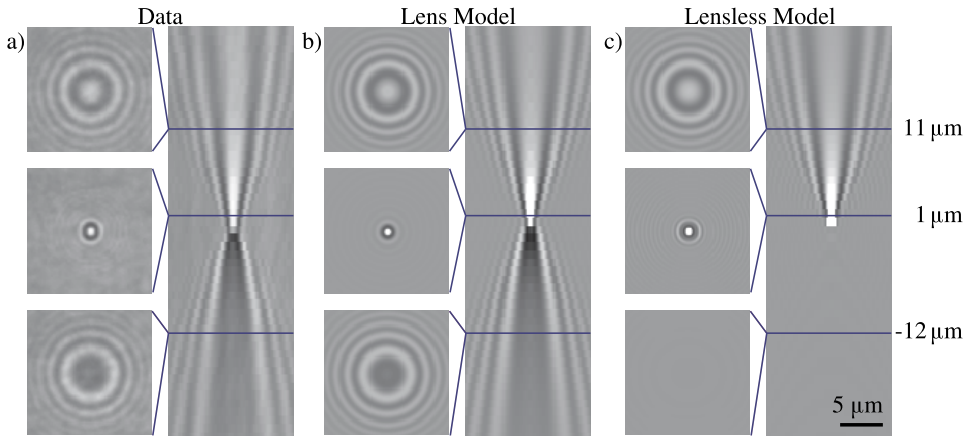

Fig. 2. Comparison of (a) experimental holograms of a 1-μm-diameter polystyrene particle in an acrylamide gel to predictions from (b) the lens model and (c) lensless model, over a range of particle z_p positions. The left half of each panel shows holograms for a particle 11 μm above, 1 μm above, and 12 μm below the focal plane of the objective, while the right half of each panel shows xz-cross-sections as a function of the focal position, where each cross-section is the intensity of the hologram across a line running through the center of the central lobe. All images are shown at the same scale. The lensless model cannot predict the recorded holograms when the particle is in or below the focus.

To test how the lens model performs in a 3D particle tracking experiment, we record a movie of a 2.4-μm-diameter polystyrene particle sedimenting in water. The particle starts tens of micrometers above the focus and sediments through the focus as it diffuses. We do not change the focus of the objective during the experiment. We measure the particle's trajectory by fitting the lens model to each frame of the video, fitting for the particle's 3D position, radius, and refractive index, as well as the objective's acceptance angle β and the field rescaling parameter α. For comparison, we also fit the lensless model to the data when the particle is above the focal plane, fitting for the particle's 3D position, radius, and refractive index, as well as the field rescaling parameter α. We then compare the particle trajectories inferred from the two models to each other and to the sedimentation velocity predicted from Stokes's law (Fig. 3).

Both above and below the focus, the trajectory inferred using the lens model is consistent with that expected from Stokes's law for a diffusing, sedimenting particle. We measure a sedimentation velocity of 0.18 ± 0.06 μm/s, where the uncertainty is primarily from the particle's diffusion. We predict a velocity of 0.18 ± 0.04 μm/s, where the uncertainty is primarily from limited knowledge of the particle radius.

When the particle is well above the focus, the positions that we infer using the lens model agree quantitatively with those we infer using the lensless model. However, when the particle is within 3 μm of the focus, the best-fit holograms from the lensless model fail to reproduce the recorded images. Instead, the best fits from the lensless model converge to $\alpha = 0$, corresponding to a structureless hologram.

Fitting the model to the data also provides estimates for the particle index, radius, field rescaling parameter α, and objective acceptance angle β, as shown in Fig. 4. Well above the focus, both the lens and lensless models provide similar values for these parameters. Moreover, the inferred index and radius from both models agree with those provided by the manufacturer. The inferred lens acceptance angle is not well constrained by the fits. Given that the lensless model can fit the data in this region, the large uncertainty in the lens angle makes sense. When the particle is well

Optics EXPRESS

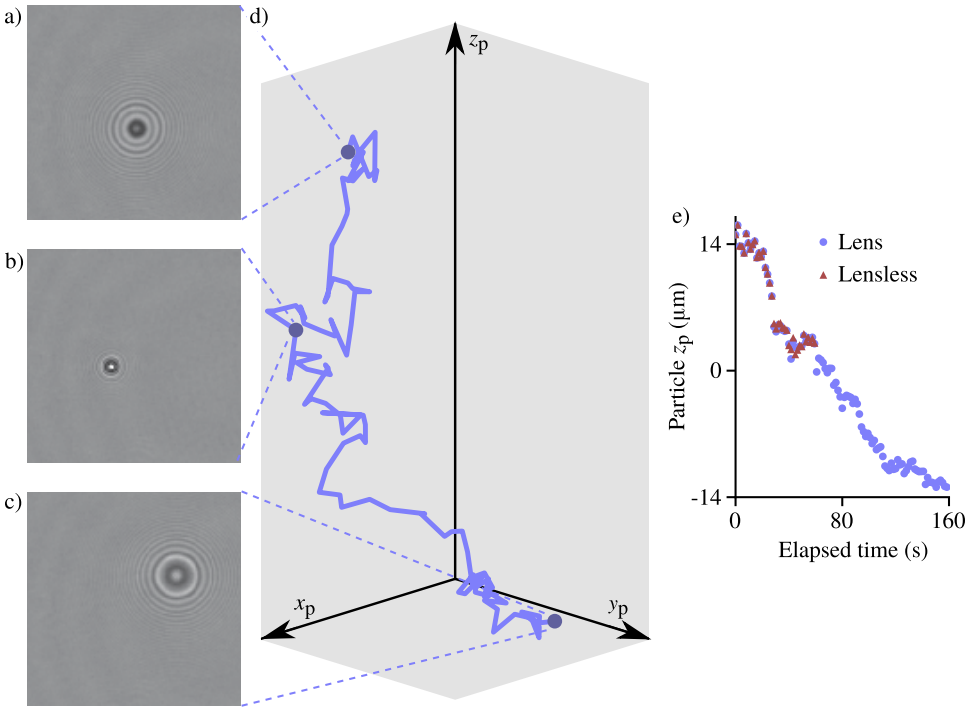

Fig. 3. 3D tracking of a 2.4-μm-diameter polystyrene sphere as it diffuses and sediments through the focus of the objective to the coverslip located approximately 15 μm below the focal plane. Images show recorded holograms (a) well above the focus, (b) near the focus, and (c) well below the focus. From the recorded holograms, we reconstruct (d) the particle's 3D trajectory, including (e) its height above the focus z_p as a function of time. Using the lensless model, we track the particle only above the focus (red triangles in (e)). By modeling the lens, we extend the range of particle tracking to within and below the focus (trajectory in (d) and blue circles in (e).

below the focus (where the lensless model does not apply), the particle index and radius inferred through the lens model are similar to those inferred when the particle is well above the focus.

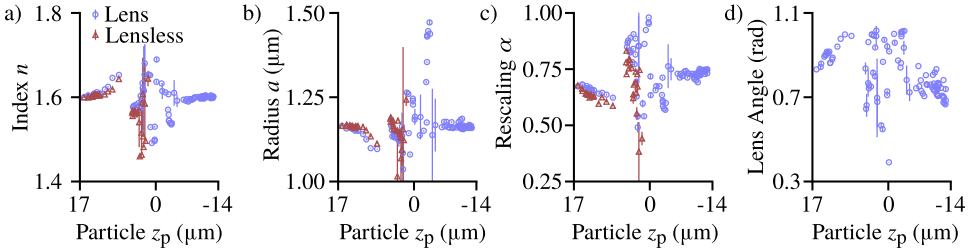

Fig. 4. Particle and optical-train characterization results for the same images in Fig. 3. For each particle z_p, we infer the particle refractive index (a), the particle radius (b), the field rescaling parameter α (c), and the acceptance angle β of the microscope objective (d). The results from the lens model are shown in blue circles and those from the lensless model in red triangles. Error bars show the *a posteriori* standard deviation. The acceptance angle of the objective is a parameter only in the lens model.

Optics EXPRESS

However, as the particle nears the focus, the characterization results worsen for both models. The reported particle refractive index and radius fluctuate with z_p. Also, the fit landscape for the lens model is multimodal near the focus. We hypothesize that this poor characterization near the focus is intrinsic to holograms recorded near the focal plane, since the particle properties are inferred primarily from the fringes, and the fringe pattern disappears near the focus.

There are differences between holograms predicted by the lensless model and those predicted by the lens model even when the particle is above the focal plane. These differences are shown in Fig. 5. When the particle is 10 μm above the focus, a hologram simulated with the lensless model is visually indistinguishable from one simulated with the lens model for a high-NA lens (Fig. 5(a)). However, as either the NA decreases (Fig. 5(b)) or the particle approaches the focus (Fig. 5(c)), the two models differ in their predictions, particularly in the fringe spacing and contrast. When the particle is close to the focal plane and imaged with a low-aperture lens, the difference in fringe spacing predicted by the models becomes dramatic (Fig. 5(d)). Furthermore, in this case the lens model predicts a dark central lobe, while the lensless model predicts a bright one (Fig. 5(d)).

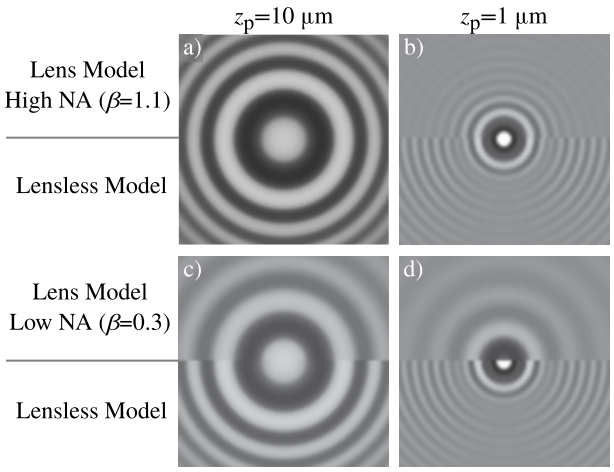

Fig. 5. Even above the focus, predictions for the hologram differ between the lens and lensless models. We show simulated holograms of a 1-μm-diameter polystyrene sphere in water illuminated with 660-nm-wavelength light for (a) particle height z_p = 10 μm above the focus and lens acceptance angle β = 1.1, (b) z_p = 1 μm and β = 1.1, (c) z_p = 10 μm and β = 0.3, and (d) z_p = 1 μm and β = 0.3. The upper half of each image shows the hologram simulated with the lens model, and the lower half shows the simulation from the lensless model. The contrast has been nonlinearly adjusted to highlight the fringes, using a gamma of 0.5 for intensities above and below the hologram background intensity. The field of view of each image is 5 × 5 μm.

A dark central lobe near the focus is more physically realistic than a bright one: as the particle passes through the focus, the Gouy phase shift must lead to an inversion of the contrast of the hologram's central lobe, as is well appreciated in both brightfield and holographic microscopy [26,27]. When the particle is far above the focal plane, the scattered beam comes to a focus behind the detector and does not have a Gouy phase shift at the detector plane. But as the particle passes below the focal plane, the scattered beam comes to a focus in front of the detector, smoothly accumulating a Gouy phase shift. While the exact phase shift for the scattered beam as predicted by Eqs. (8)–(10) is more complex than the simple Gouy phase shift of π for a plane wave, the two are qualitatively similar. Thus, the central fringe should become dark near and below the focus, as predicted by the lens model and as shown in our measurements (Fig. 2(a)). The lensless

Optics EXPRESS

model predicts no change in contrast as the particle nears the focus, because it predicts no change in phase of the forward-scattered beam relative to the incident beam as z_p changes.

To understand why the fringe spacing differs between the two models, we consider the effect of the lens acceptance angle β on the fringe spacing. The lens model predicts that near the focus the fringe spacing should increase significantly with decreasing β, as shown in Fig. 6. In the lens model, this increase in fringe spacing is due to the point-spread function. A lens images slowly-varying electric fields but blurs out any features with periodicity less than the objective's resolution limit $\lambda/\mathrm{NA} = \lambda/n_f \sin\beta$. As a result, the smallest possible fringe spacing in a hologram from the lens model is λ/NA, larger than the smallest possible fringe spacing of λ in the lensless model. This difference is especially noticeable when the fringes are closely spaced, as happens either far from the hologram's center or when the particle is near the focus.

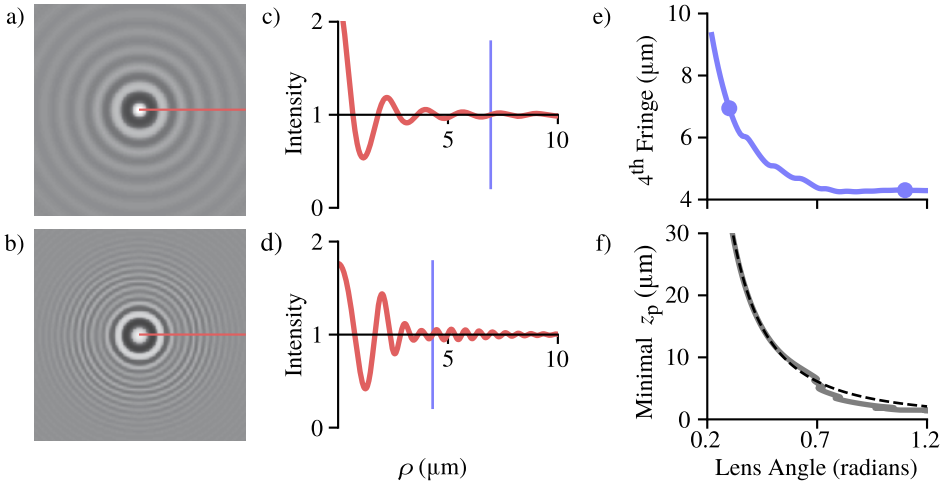

Fig. 6. Simulations from the lens model show the effect of lens angle on the fringe spacing in a recorded hologram. (a, b) Holograms for a 1.0-μm-diameter polystyrene particle $z_p = 5$ μm above the focal plane, simulated from the lens model with an acceptance angle of $\beta = 0.3$ (a) and $\beta = 1.1$ (b). The contrast is nonlinearly adjusted to highlight the fringes, as described in Fig. 5. (c, d) The normalized intensity of the holograms in (a) and (b), respectively, plotted against distance from the particle center. We determine the location of the fourth fringe as the point where the intensity crosses the ρ-axis immediately before the fourth maximum (blue lines). (e) Calculated location of the fourth fringe as a function of lens acceptance angle for a 1.0-μm-diameter polystyrene sphere located 5 μm above the focal plane. The two circles highlight the fringe spacings in (c) and (d). (f) Minimum height z_p at which the location of the fourth fringe predicted by the lensless model is within 2% of its value in the lens model (solid gray line). The dashed black line shows the 3.0 μm / β^2 scaling.

The variation of the fringe spacing with lens acceptance angle can lead to systematic errors when one uses the lensless model to infer the particle position from a measured hologram. To illustrate this point, we quantify the change in fringe spacing as a function of the lens acceptance angle. Specifically, we calculate the distance from the hologram's central lobe to the fourth fringe (Figs. 6(a)–6(d)) in simulated holograms of a 1.0-μm-diameter polystyrene sphere in water at $z_p = 5$ μm. According to the lens model, the distance from the central lobe to the fourth fringe changes significantly with the lens acceptance angle β, from 6.9 μm when $\beta = 0.3$ to 4.3 μm when $\beta = 1.1$ (Fig. 6(e)). Because information about the particle height z_p is contained primarily in the fringe spacing, and because the lensless model does not account for the change in fringe spacing due to the objective's limited resolution, using the lensless model to infer z_p from a measured hologram will lead to a systematic error.

Optics EXPRESS

To determine the imaging conditions under which this systematic error is significant, we calculate the minimum particle z_p at which a hologram predicted by the lensless model agrees with that of the lens model (Fig. 6(f)), as quantified by the difference in the fourth fringe position. As the particle approaches the focus, the scattered electric field in the focal plane varies on finer and finer scales. When the particle is closer than a certain z_p, the field varies on a finer scale than the objective's resolution limit λ/NA, and the resolution limit rather than z_p sets the fringe spacing in the lens model. At this z_p, the lens and lensless models predict different holograms. For a lens with $\beta = 0.3$ (corresponding to an NA of 0.4 for a water-immersion objective), the particle z_p must be at least 20 μm above the focus for the two models to agree. As the lens acceptance angle increases to $\beta = 0.8$ (NA of 1.0 for water-immersion), the particle can be as low as 5 μm above the focus before the fringe spacing differs significantly from that predicted by the lensless model.

The lensless model omits two effects: the Gouy phase shift and the objective's resolution limit. Both of these effects are important when the particle is within the objective's depth of field: the phase shift because the scattered beam's waist straddles the detector, and the resolution limit because the hologram's structure varies rapidly. In fact, we find that the minimal z_p for a hologram to be accurately described by the lensless model scales as $3\,\mu\mathrm{m}/\beta^2$ (Fig. 6(f)), proportional to the theoretical scaling of the objective's depth of field [26,32].

Modeling the lens also resolves a puzzle about holographic imaging of particles near the focus: the lensless model requires the near-field dependence of the scattered field to predict the hologram accurately [3,22,23], even though the detector is hundreds of millimeters downstream of the lens, well in the far field. For a 1 μm-diameter particle 15 μm above the focus, holograms calculated by the lensless model which use the far-field approximation deviate by 10% from those which use the full near-field dependence [33]. Why does the near-field form provide a better approximation than the far-field solution? The reason is that the far-field form of the electric field as predicted by the lensless model is only an approximate solution to the wave equation, not an exact solution. In contrast, the near-field form is an exact solution to the wave equation, albeit for a different imaging setup than used in holographic microscopy. By constraining the field to be an exact solution to the wave equation, the near-field version of the lensless model describes the actual hologram more closely than the far-field version does. By contrast, the electric field predicted by the lens model is an exact solution to the wave equation for the imaging setup.

4. Conclusion

We have presented a model that accounts for the effect of an aberration-free objective lens on in-line holograms of isolated spherical particles, and we show that the fringe spacing and contrast depend strongly on the lens acceptance angle. This variation agrees well with that observed experimentally above, near, and below the focus of the objective. We have shown also that the lens model can be used to infer the 3D position of a colloidal sphere near and below the focus of the objective, effectively doubling the depth of field as compared to the lensless model. Furthermore, because the model accounts for the effect of the lens aperture on the fringe spacing, it can be used to infer the height of the particle from a measured hologram with lower systematic error, even above the focus.

By capturing physical effects of the lens such as the change in phase of the scattered beam on passing through the focus, our results also provide insight into holograms of more complex scatterers. While the compact representation that we derive in Eq. (12) is applicable to either isolated spheres or well-separated collections of spheres [22], the corresponding expression is not so compact for more complex scatterers, such as ellipsoids or compact clusters of spheres. Nevertheless, we expect that the qualitative behavior shown in Figs. 5 and 6 will still hold, and that a lensless model will accurately describe the recorded hologram so long as the scatterer is outside the objective's depth of focus. The lens model can be used to quantitatively estimate this

Optics EXPRESS

minimum height as a function of the numerical aperture of the objective. Therefore, the model is useful not only for fitting holograms of spherical scatterers, but also for determining the range of validity of general lensless models, which are easier to implement computationally.

For spherical particles, all the physics described by the lens model is also described in the earlier work of [17]. However, our simplified model requires the calculation of only the integrals $\mathcal{I}_0$ and $\mathcal{I}_2$ in Eqs. (9) and (10), allowing for a straightforward and efficient computational implementation. We find that calculating a hologram with the lens model takes roughly the same time as with the lensless model, because much of the time is spent computing the Mie scattering matrices. With the numerical optimizations detailed in Appendix A, the implementation of the lens model becomes three times as fast as the lensless model. This fast implementation is available in the open-source package `holopy` [34].

Appendix A: Numerical methods

Calculating a hologram of shape $N \times N$ with the lens model for a single particle involves numerically integrating Eqs. (9)–(10) over each of the N^2 values of ρ_p in the image. We perform this integration through Gauss-Legendre quadrature over $\cos\theta_o$. For large ρ_p, the $J_n(u\sin(\theta_o))$ terms oscillate rapidly and require many quadrature points for accurate integration; empirically, we find 100 quadrature points provides good accuracy for $k\rho_p$<400. Because the Mie scattering coefficients $S_\parallel(\theta)$ and $S_\perp(\theta)$ do not depend on ρ_p or z_p, we pre-compute the scattering coefficients once at the quadrature nodes and use these values for each of the separate integrations over ρ_p. With the pre-computed scattering coefficients, the slowest part of the integration is the computation of the Bessel functions at the N^2 values of ρ_p. Since the maximum ρ_p is only of $O(N)$, we reduce this near-redundant computation by creating an interpolator for $\mathcal{I}_n$. Interpolating $\mathcal{I}_n$ with piecewise Chebyshev interpolators of degree 32 over windows of size $\Delta u = 39$ provides a fifteen-fold speed increase, with a relative accuracy on the order of 10^{-12}. With these optimizations, directly calculating a 256×256 hologram on an Intel Core i7 (single-threaded process at 3.5 GHz) takes 50 ms, with an additional 30 ms for overhead incurred by `holopy`. We also use `holopy` to calculate the lensless model, using methods described in [34].

To fit the models to the sedimentation data, we use a combination of nonlinear least-squares fitting via the Levenberg-Marquardt algorithm and Monte-Carlo sampling. The Levenberg-Marquardt algorithm is fast, generating results from individual holograms in seconds. However, we find that there can be multiple maxima in the posterior probability distribution for the lens model, and in this situation the Levenberg-Marquardt algorithm may not find the global maximum. This multimodality depends on the extent of the hologram that is fitted: fitting the model to a larger region partially smooths out the multiple maxima. To minimize the multimodality in the fits, we fit both models to 256×256 pixel (43.4×43.4 μm) windows. To help ensure that we find the global posterior maximum, we fit the holograms using a parallel-tempered [35], affine-invariant [36], Markov-chain Monte Carlo ensemble sampler, as implemented in the Python package `emcee` [37]. Running a parallel tempering algorithm at 7 temperatures with 128 walkers for 1024 steps takes approximately 2 hours per hologram on a 32-core machine. We find that parallel tempering improves particle tracking and characterization by avoiding local minima in the posterior landscape.

We validate the numerical implementation of Eqs. (8)–(12) with the following test derived from using conservation of energy of the scattered beam. The power scattered from the particle crossing the surface S_o must be equal to that striking the detector plane. By construction, the Poynting vector is perpendicular to S_o, so the flux on S_o is $|\mathbf{E}_{S_o}|^2/c$. Substituting the field from a Mie scatterer (Eqs. (3) and (7)) and integrating over ϕ_o gives the power on S_o:

$$P_{S_o} = \frac{\pi}{c}\frac{|E_0|^2}{k^2}\int_0^\beta \left[|S_\parallel(\theta)|^2 + |S_\perp(\theta)|^2\right]\sin\theta_o d\theta_o. \tag{13}$$

Optics EXPRESS

To the accuracy of the approximations, the Poynting vector is perpendicular to the detector plane, and the flux on the detector is $|\mathbf{E}_{\mathrm{sc,det}}|^2/c$. Substituting the scattered field from Eq. (8) and integrating over ϕ_{det} gives

$$P_{\mathrm{det}} = \frac{\pi}{2c}\frac{|E_0|^2}{M^2}\int_0^\infty \left[|\mathcal{I}_0(k\rho_{\mathrm{det}}/M; kz_{\mathrm{p}})|^2 + |\mathcal{I}_2(k\rho_{\mathrm{det}}/M; kz_{\mathrm{p}})|^2\right]\rho_{\mathrm{det}}\, d\rho_{\mathrm{det}}. \tag{14}$$

Equating the powers in Eqs. (13) and (14) and substituting $u \equiv k\rho_{\mathrm{det}}/M$ in Eq. (14) relates the scattered field on the detector plane to the scattering matrix as

$$\int_0^\beta \left[|S_{\parallel}(\theta)|^2 + |S_{\perp}(\theta)^2|\right]\sin\theta\, d\theta = \frac{1}{2}\int_0^\infty \left[|\mathcal{I}_0(u, kz_{\mathrm{p}})|^2 + |\mathcal{I}_2(u, kz_{\mathrm{p}})|^2\right] u\, du. \tag{15}$$

We use this integral relationship as a unit test of our numerical implementation of the scattered field, testing the implementation over a range of lens acceptance angles, particle positions, particle refractive indices, and particle radii. The analogous test for conservation of total energy in the scattered and incident beams is not numerically practical; however, one can show that conservation of energy combined with Eqs. (12) yields the optical theorem.

Appendix B: Experimental methods

The data in Fig. 2 were obtained on a sample of colloidal spheres in a polyacrylamide hydrogel prepared by free radical polymerization. To make the hydrogel, we first combine 2 parts water and 1 part Protogel (30% w/v acrylamide, 0.8% w/v bis-acrylamide, National Diagnostics). We then mix 27 µL of the Protogel mixture with 1.5 µL of a 10^{-4}% w/v suspension of 1.0-µm-diameter polystyrene spheres (Polysciences 19404) in water and with 0.2 µL of the UV polymerization initiator Darocur 1173 (2-hydroxy-2-methylpropriophenone, Aldrich). We place the mixture in a sample cell composed of glass slides separated by a 50 µm thick spacer, seal the edges of the cell with vacuum grease, and irradiate the cell with an ultraviolet lamp to cure the hydrogel. This procedure produces a transparent polyacrylamide hydrogel with refractive index of 1.348, as measured by an Abbe refractometer. To prevent the hydrogel from drying during the experiment, we fill the chamber surrounding the gel with water using a syringe inserted through the vacuum grease. We then image the particle at 51 defocus positions spanning 50 µm, centered on the particle. Details of the imaging setup are given below.

For the sedimentation experiment in Fig. 3, we image a dilute suspension of polystyrene microspheres with a reported diameter of 2.4 µm (density 1.055 g/mL, index 1.591 at 590 nm, Invitrogen S37502). We prepare a 10^{-4} % w/v colloidal suspension and place it in a sample chamber made of a glass coverslips separated by 50-µm-thick plastic spacers. We invert the sample chamber for several minutes to give the particles time to sediment to the top coverslip, then place the sample chamber right-side up onto the microscope. We adjust the focal position of the objective to be within the sample chamber and image the particles as they sediment through the focus.

In both experiments, the imaging setup consists of a Nikon Eclipse Ti TE2000 microscope with a water-immersion objective (Plan Apo VC 60×/1.20 WI, Nikon), with the correction collar set to the thickness of the coverslip to minimize aberrations. The images in Fig. 2 are obtained from a 1280×1024-pixel CMOS color sensor array (Edmund Optics 1312C) and in Fig. 3 from a 1024×1024-pixel CMOS monochrome sensor array (PhotonFocus A1024). After obtaining images of each particle, we record a set of background images by moving the particle out of the field of view in several directions. The raw holograms are processed prior to fitting by dividing by the average background intensity. In addition, we take dark-count data by acquiring images with the primary light source switched off. We average these dark-count images and subtract them from the background-corrected data before analysis.

Optics EXPRESS

Funding

National Science Foundation (DMR-1420570).

Acknowledgments

We thank G. Keshavarzi, A. Goldfain, R. Perry, T. Dimiduk, J. Fung, and A. Small for useful discussions.

Disclosures

The authors declare no conflicts of interest.

References

1. S.-H. Lee, Y. Roichman, G.-R. Yi, S.-H. Kim, S.-M. Yang, A. van Blaaderen, P. van Oostrum, and D. G. Grier, "Characterizing and tracking single colloidal particles with video holographic microscopy," Opt. Express **15**(26), 18275–18282 (2007).
2. J. Sheng, E. Malkiel, and J. Katz, "Digital holographic microscope for measuring three-dimensional particle distributions and motions," Appl. Opt. **45**(16), 3893–3901 (2006).
3. J. Fung, K. E. Martin, R. W. Perry, D. M. Kaz, R. McGorty, and V. N. Manoharan, "Measuring translational, rotational, and vibrational dynamics in colloids with digital holographic microscopy," Opt. Express **19**(9), 8051–8065 (2011).
4. J. Fung and V. N. Manoharan, "Holographic measurements of anisotropic three-dimensional diffusion of colloidal clusters," Phys. Rev. E **88**(2), 020302 (2013).
5. D. M. Kaz, R. McGorty, M. Mani, M. P. Brenner, and V. N. Manoharan, "Physical ageing of the contact line on colloidal particles at liquid interfaces," Nat. Mater. **11**(2), 138–142 (2012).
6. K. D. Hinsch, "Holographic particle image velocimetry," Meas. Sci. Technol. **13**(7), R61–R72 (2002).
7. J. Garcia-Sucerquia, W. Xu, S. Jericho, M. Jericho, and H. J. Kreuzer, "4-D imaging of fluid flow with digital in-line holographic microscopy," Optik **119**(9), 419–423 (2008).
8. A. Wang, R. F. Garmann, and V. N. Manoharan, "Tracking *E. coli* runs and tumbles with scattering solutions and digital holographic microscopy," Opt. Express **24**(21), 23719–23725 (2016).
9. A. Khmaladze, M. Kim, and C.-M. Lo, "Phase imaging of cells by simultaneous dual-wavelength reflection digital holography," Opt. Express **16**(15), 10900–10911 (2008).
10. Y.-S. Choi and S.-J. Lee, "Three-dimensional volumetric measurement of red blood cell motion using digital holographic microscopy," Appl. Opt. **48**(16), 2983–2990 (2009).
11. B. Kemper and J. Schnekenburger, "Digital holographic microscopy for quantitative live cell imaging and cytometry," in "Advanced optical flow cytometry: methods and disease diagnoses," V. V. Tuchin, ed. (Wiley-VCH Verlag & Co., Weinheim, Germany, 2011), pp. 211–237.
12. P. Marquet, B. Rappaz, P. J. Magistretti, E. Cuche, Y. Emery, T. Colomb, and C. Depeursinge, "Digital holographic microscopy: a noninvasive contrast imaging technique allowing quantitative visualization of living cells with subwavelength axial accuracy," Opt. Lett. **30**(5), 468–470 (2005).
13. D. Gabor, "A new microscopic principle," Nature **161**(4098), 777–778 (1948).
14. U. Schnars and W. P. Jüptner, "Digital recording and numerical reconstruction of holograms," Meas. Sci. Technol. **13**(9), R85–R101 (2002).
15. J. Garcia-Sucerquia, W. Xu, S. K. Jericho, P. Klages, M. H. Jericho, and H. J. Kreuzer, "Digital in-line holographic microscopy," Appl. Opt. **45**(5), 836–850 (2006).
16. Y. Pu and H. Meng, "Intrinsic aberrations due to Mie scattering in particle holography," J. Opt. Soc. Am. A **20**(10), 1920–1932 (2003).
17. B. Ovryn and S. H. Izen, "Imaging of transparent spheres through a planar interface using a high-numerical-aperture optical microscope," J. Opt. Soc. Am. A **17**(7), 1202–1213 (2000).
18. F. C. Cheong, B. J. Krishnatreya, and D. G. Grier, "Strategies for three-dimensional particle tracking with holographic video microscopy," Opt. Express **18**(13), 13563–13573 (2010).
19. B. J. Krishnatreya, A. Colen-Landy, P. Hasebe, B. A. Bell, J. R. Jones, A. Sunda-Meya, and D. G. Grier, "Measuring Boltzmann's constant through holographic video microscopy of a single colloidal sphere," Am. J. Phys. **82**(1), 23–31 (2014).
20. M. J. O'Brien and D. G. Grier, "Above and beyond: holographic tracking of axial displacements in holographic optical tweezers," Opt. Express **27**(18), 25375–25383 (2019).
21. T. G. Dimiduk and V. N. Manoharan, "Bayesian approach to analyzing holograms of colloidal particles," Opt. Express **24**(21), 24045–24060 (2016).
22. J. Fung, R. W. Perry, T. G. Dimiduk, and V. N. Manoharan, "Imaging multiple colloidal particles by fitting electromagnetic scattering solutions to digital holograms," J. Quant. Spectrosc. Radiat. Transfer **113**(18), 2482–2489 (2012).

Optics EXPRESS

23. A. Wang, T. G. Dimiduk, J. Fung, S. Razavi, I. Kretzschmar, K. Chaudhary, and V. N. Manoharan, "Using the discrete dipole approximation and holographic microscopy to measure rotational dynamics of non-spherical colloidal particles," J. Quant. Spectrosc. Radiat. Transfer **146**, 499–509 (2014).
24. S. Feng and H. G. Winful, "Physical origin of the Gouy phase shift," Opt. Lett. **26**(8), 485–487 (2001).
25. E. Atılgan and B. Ovryn, "Reflectivity and topography of cells grown on glass-coverslips measured with phase-shifted laser feedback interference microscopy," Biomed. Opt. Express **2**(8), 2417–2437 (2011).
26. J. Mertz, *Introduction to optical microscopy* (Cambridge University Press, 2019).
27. L. Wilson and R. Zhang, "3D localization of weak scatterers in digital holographic microscopy using Rayleigh-Sommerfeld back-propagation," Opt. Express **20**(15), 16735–16744 (2012).
28. S. Hell, G. Reiner, C. Cremer, and E. H. Stelzer, "Aberrations in confocal fluorescence microscopy induced by mismatches in refractive index," J. Microsc. **169**(3), 391–405 (1993).
29. B. Richards and E. Wolf, "Electromagnetic diffraction in optical systems, II. Structure of the image field in an aplanatic system," Proc. R. Soc. Lond. A **253**(1274), 358–379 (1959).
30. T. D. Visser and S. H. Wiersma, "Spherical aberration and the electromagnetic field in high-aperture systems," J. Opt. Soc. Am. A **8**(9), 1404–1410 (1991).
31. H. C. van de Hulst, *Light scattering by small particles* (Dover Publications, 1981).
32. M. Born and E. Wolf, *Principles of Optics* (Cambridge University Press, 1983), 3rd ed.
33. J. Fung, "Measuring the 3D dynamics of multiple colloidal particles with digital holographic microscopy," Ph.D. thesis, Harvard University (2013).
34. S. Barkley, T. Dimiduk, J. Fung, D. Kaz, V. N. Manoharan, R. McGorty, R. Perry, and A. Wang, "Holographic microscopy with Python and HoloPy," *Comput. Sci. Eng.* (2019).
35. D. J. Earl and M. W. Deem, "Parallel tempering: Theory, applications, and new perspectives," Phys. Chem. Chem. Phys. **7**(23), 3910–3916 (2005).
36. J. Goodman and J. Weare, "Ensemble samplers with affine invariance," Comm. App. Math. Comp. Sc. **5**(1), 65–80 (2010).
37. D. Foreman-Mackey, D. W. Hogg, D. Lang, and J. Goodman, "emcee: the MCMC hammer," Publ. Astron. Soc. Pac. **125**(925), 306–312 (2013).